The Large-Scale Vorticity Balance of the Antarctic Continental Margin in a Fine-Resolution Global Simulation

ANDRÉ PALÓCZY, JULIE L. MCCLEAN, SARAH T. GILLE, AND HE WANG[a]

Scripps Institution of Oceanography, La Jolla, California

(Manuscript received 4 December 2019, in final form 26 May 2020)

ABSTRACT

The depth-integrated vorticity budget of a global, eddy-permitting ocean/sea ice simulation over the Antarctic continental margin (ACM) is diagnosed to understand the physical mechanisms implicated in meridional transport. The leading-order balance is between the torques due to lateral friction, nonlinear effects, and bottom vortex stretching, although details vary regionally. Maps of the time-averaged depth-integrated vorticity budget terms and time series of the spatially averaged, depth-integrated vorticity budget terms reveal that the flow in the Amundsen, Bellingshausen, and Weddell Seas and, to a lesser extent, in the western portion of East Antarctica, is closer to an approximate topographic Sverdrup balance (TSB) compared to other segments of the ACM. Correlation and coherence analyses further support these findings, and also show that inclusion of the vorticity tendency term in the response (the planetary vorticity advection and the bottom vortex stretching term) increases the correlation with the forcing (the vertical net stress curl), and also increases the coherence between forcing and response at high frequencies across the ACM, except for the West Antarctic Peninsula. These findings suggest that the surface stress curl, imparted by the wind and the sea ice, has the potential to contribute to the meridional, approximately cross-slope, transport to a greater extent in the Amundsen, Bellingshausen, Weddell, and part of the East Antarctic continental margin than elsewhere in the ACM.

1. Introduction

The circulation over the Antarctic continental margin (ACM) mediates the exchange of mass and heat between the Southern Ocean and the coast, particularly where the Antarctic Slope Front (ASF) occurs. It is thus a key player in the ocean's global overturning circulation and in Earth's climate system (e.g., Thompson et al. 2018). The processes responsible for this exchange are also relevant for understanding and predicting global sea level change. Heat brought from offshore by relatively warm Circumpolar Deep Water (CDW) intrudes onto the continental shelf and underneath the ice shelves' subglacial cavities (e.g., Jacobs et al. 2011; Nøst et al. 2011; Rintoul et al. 2016; Silvano et al. 2016, 2017; Castagno et al. 2017; Mallett et al. 2018) and is the major contributor to the observed mass loss rates of the ice shelves that buttress the Antarctic Ice Sheet (Rignot et al. 2013; Depoorter et al. 2013). Understanding the large-scale dynamics driving these processes and how they manifest themselves in climate and Earth System models is thus of primary societal importance.

Dynamically, the problem is to identify the processes responsible for breaking the Taylor–Proudman constraint, which posits that purely geostrophic flow on an f plane must follow isobaths (e.g., Brink 2016), or in the case of variable f, contours of f/h, where f is the Coriolis parameter and h is the ocean depth (e.g., Holland 1973; Mertz and Wright 1992; Holloway 2008). The vorticity balance offers a useful dynamical framework for studying cross-f/h transport processes for two reasons: first, it filters out large horizontal pressure gradients associated with the geostrophic balance, which are not physically insightful by themselves because they can be caused by several different mechanisms, and second, it is insensitive to the choice of rotation angle, unlike the cross-isobath velocity in the along-isobath momentum balance (Brink 2016). The insensitivity to rotation angle is particularly important in complicated geometries such as that of the ACM (Stewart et al. 2018, 2019). In regions

[a] Current affiliation: Argonne National Laboratory, Lemont, Illinois.

Corresponding author: André Palóczy, apaloczy@ucsd.edu

DOI: 10.1175/JPO-D-19-0307.1

where the ACM is predominantly zonally oriented, the planetary vorticity advection term (βV, where β is the planetary vorticity gradient and V is the vertically integrated meridional velocity) in the depth-integrated vorticity equation is an approximate metric for cross-slope transport. This was exploited by Rodriguez et al. (2016), who found a net transport of ~1 Sv (1 Sv $\equiv 10^6\,m^3\,s^{-1}$) into the Amundsen Sea embayment associated with the 2005–10 time-mean cyclonic wind stress curl in the Southern Ocean State Estimate (SOSE).

Some previous diagnostic studies of the large-scale vorticity budget in coarse (Lu and Stammer 2004; Yeager 2013, 2015) and eddy-permitting (Hughes and de Cuevas 2001) models have examined the role of bottom pressure torques or bottom vortex stretching in driving the depth-integrated circulation patterns in the vicinity of sloping topography, as first discussed for a stratified square basin with sloping sidewalls by Holland (1973). A common thread in these studies is that regions with relatively flat topography are diagnosed to be closer to Sverdrup balance as predicted by classical idealized theories (see also Wunsch 2011), while depth-integrated flow close to steep topography is found to be strongly influenced by bottom pressure torques (Hughes and de Cuevas 2001; Lu and Stammer 2004; Yeager 2013, 2015). At shorter time scales, one may also expect the relative vorticity tendency term to be important, further complicating the vorticity balance. Examination of the validity and localization of these simplified dynamical balances in the ACM is the central goal of this study.

A major circulation feature of the ACM is the Antarctic Slope Current (ASC), an extensive current encircling most of Antarctica, associated with the ASF and thought to act as a mediator of cross-slope transport (e.g., Thompson et al. 2018). Recent modeling work suggests that the ASC's jet is mostly driven by tidal momentum flux convergences at the shelf break in the Weddell–Scotia confluence (e.g., Flexas et al. 2015), and possibly along its entire extension around the continent (Stewart et al. 2019). Its variability is also known to be sensitive to large-scale wind forcing associated with climate modes such as the southern annular mode (e.g., Armitage et al. 2018; Thompson et al. 2018). Therefore, in a changing climate, modified large-scale wind patterns may produce regional differences in these heat exchanges, to the degree that they control the circulation in the ACM. Another important circulation feature is the Antarctic Coastal Current, which flows westward hugging the coast in some sectors of the ACM, such as the Western Antarctic Peninsula, where it is usually called the Antarctic Peninsula Coastal Current (e.g., Moffat and Meredith 2018). In this study, we focus on the localization and temporal variability of the vorticity balances that drive meridional flow through the planetary vorticity advection term βV, partly contributing to cross-isobath transport across the continental shelf and slope of the ACM, rather than on the dynamics of a particular circulation feature, such as the ASC or the Antarctic Coastal Current.

The purpose of this study is to investigate the dynamics of the cross-slope transport in the geostrophic interior along the ACM through the lens of a vorticity budget. Specifically, we aim to test the hypothesis that a simplified Sverdrup-like vorticity balance accounts for some of the meridional mass and heat transports (both downslope and upslope), in an eddy-permitting global ocean model. Although transports within the surface and bottom Ekman layers may not be negligible around the entire continental margin (e.g., Thompson et al. 2014; Silvano et al. 2016), the water mass that makes the largest contribution to the onshelf heat transport (CDW) occupies the geostrophic interior of the water column, with a core typically at ~300–600 m depth along the continental slope (e.g., Schmidtko et al. 2014; Thompson et al. 2018). Although a large fraction of this transport is due to eddies (Stewart and Thompson 2015; Palóczy et al. 2018; Stewart et al. 2018, 2019), part of the time-mean component of the meridional, cross-slope transport (both onshore and offshore, Goddard et al. 2017; Palóczy et al. 2018) should be captured by a local Sverdrup-like balance.

The remainder of the paper is organized as follows. We begin by explaining the methodology used to diagnose the vorticity budget from our numerical simulation in section 2. We then present the results of the analyses of the time-averaged (section 3) and time-varying (section 4) vorticity budgets, and discuss our findings and conclusions in section 5.

2. Formulation of the vorticity diagnostics

We use a 0.1°-resolution global simulation with 42 vertical levels that couples the Los Alamos Parallel Ocean Program 2 (POP2; e.g., Smith et al. 2010) with the Los Alamos Community Ice Code 4 (CICE4; e.g., Hunke and Lipscomb 2010) in the Community Earth System Model 1.2 (CESM 1.2) framework to diagnose the vorticity budget along the ACM. The vertical resolution varies from 10 m near the surface to 500 m near the bottom. The simulation was forced by interanually varying Coordinated Ocean-Ice Reference Experiment 2 (CORE-II; Large and Yeager 2009) surface fluxes. The simulation used biharmonic horizontal viscosity and diffusivity operators, with a viscosity coefficient of $-2.7 \times 10^{10}\,m^4\,s^{-1}$ and a diffusivity coefficient of $-0.3 \times 10^{10}\,m^4\,s^{-1}$ at the equator, changing proportionally

to the cube of the grid cell size. The values of the viscosity/diffusivity coefficients are based on Smith et al. (2000), but with the diffusivity coefficient decreased by a factor of 3. Nonlocal vertical mixing of temperature and salinity was implemented with the *K*-profile parameterization (KPP; Large et al. 1994). The simulation was run for the 1948–2009 period, during which output fields were saved as monthly averages. The terms in the momentum equations (from which we calculate the vorticity budget) are available as daily averages over the period 2005–09. The simulation is described in further detail by Palóczy et al. (2018) and by McClean et al. (2018).

We first write the depth-integrated absolute vorticity equation with biharmonic lateral viscosity as

$$\underbrace{\partial_t \overline{\zeta} = \overbrace{\overbrace{-\beta \overline{v} + \nabla \times \tau_s}^{\text{SB}} - f w_b}^{\text{TSB}}}_{\text{tTSB}} - \nabla \times \tau_b - \overline{\nabla \times (\mathbf{u} \cdot \nabla \mathbf{u})} + \overline{A_H \nabla^4 \zeta}, \tag{1}$$

where overbars indicate vertical integrals, f and β are the planetary vorticity and its gradient, v is the meridional velocity, w_b and $\boldsymbol{\tau}_b$ are, respectively, the vertical velocity and horizontal kinematic stress at the bottom, $\boldsymbol{\tau}_s$ is the total surface kinematic stress (due to relative sea ice motion and wind), $\mathbf{u} \equiv \hat{\mathbf{x}} u + \hat{\mathbf{y}} v$ is the horizontal velocity vector, ζ is the vertical component of the relative vorticity vector, and A_H is the (spatially varying) lateral viscosity coefficient. The acronyms SB, TSB, and tTSB stand for Sverdrup balance, topographic Sverdrup balance, and transient topographic Sverdrup balance, respectively.

Diagnosing the depth-integrated vorticity budget in a *z*-coordinate model such as POP introduces a technical difficulty that must be overcome in order to interpret its terms analogously to those in Eq. (1). The fact that each cell has a flat bottom means that the effects of topography are masked if the terms are integrated over the full depth. However, approximate equivalence with the continuous vorticity equation can be obtained if the vertical integration is performed from the surface down to the deepest grid cell with no sidewalls, rather than to the bottom cell (Bell 1999; Yeager 2013). The result is a vertically separated vorticity budget where the terms integrated over the interior cells (i.e., away from sidewalls) may be interpreted in analogy with Eq. (1) [see the appendix for the steps between Eqs. (1) and (2)].

The vorticity budget terms are calculated from the model outputs by applying the discrete curl operator directly to the momentum budget terms, thus ensuring that the budget is numerically closed. The time-dependent term is calculated as a residual. Following Yeager (2013), we rewrite the depth-integrated vorticity budget in analogy with the momentum budget terms as

$$\begin{aligned} \mathrm{RES}_\xi = &-\mathrm{NONL}_\xi - \beta V - f w_I + \mathrm{ERRCOR} + \mathrm{PGRD}_\xi \\ &+ \mathrm{VVIS}_\xi + \mathrm{HVIS}_\xi, \end{aligned} \tag{2}$$

where the ξ subscript indicates the curl operator and the terms are, from left to right, the residual (tendency + truncation error), minus the total nonlinear term (vortex tilting and twisting + relative vorticity advection), minus the planetary vorticity advection, minus the bottom vortex stretching, an error term associated with decomposing the curl of the Coriolis term (at least an order of magnitude smaller than the next-largest terms), the pressure gradient torque (negligible away from sidewalls), the vertical viscous torque and the horizontal viscous torque. The vertical velocity at the deepest interior cell (at $z = z_I$) is w_I, and V is the vertically integrated (from $z = z_I$ to $z = 0$) meridional velocity. The continuous analog of VVIS_ξ is the total frictional torque in the geostrophic interior, i.e., $\nabla \times (\boldsymbol{\tau}_s - \boldsymbol{\tau}_b)$ in Eq. (1).

3. The time-averaged vorticity budget

We examine the regional variability of the vorticity budget by dividing the Antarctic continental slope in six segments: Ross, Amundsen–Bellingshausen (A-B), Western Antarctic Peninsula (WAP), Weddell, Western East Antarctica (W-EA), and Eastern East Antarctica (E-EA), shown in Fig. 1. Figure 2 shows that the sign of the surface stress curl [$\nabla \times \boldsymbol{\tau}_s$ in Eq. (1)] forcing the system is mostly negative, suggesting a poleward depth-integrated motion if a simple Sverdrup balance were to hold [SB in Eq. (1)]. In the following, we describe the vorticity balance and its time-averaged spatial structure in the Amundsen–Bellingshausen segment, as this segment will be shown to have its vorticity budget best approximated by a three-way balance between VVIS_ξ, $-\beta V$, and $-f w_I$.

Figure 3 shows the spatial structure of the depth-integrated vorticity budget terms in the Amundsen–Bellingshausen segment, with the associated depth-averaged velocity field overlaid in Fig. 3c. The vertical frictional torque term is generally negative across this region, except close to the coast, where the westward Antarctic Coastal Current jet is found. The spatial scales of the other terms are smaller. The magnitude of the residual and βV terms is largest beyond the continental slope, resembling the structure of the vigorous eddy field of the Antarctic Circumpolar Current (ACC) farther north.

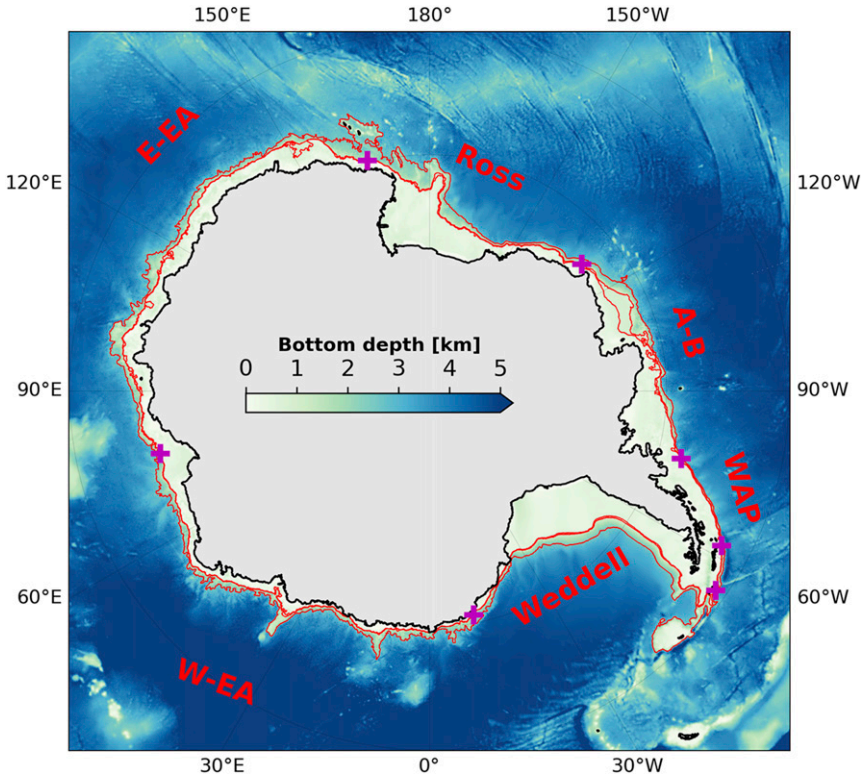

FIG. 1. Map of the model topography. The red lines are the 800, 1000, and 2500 m isobaths. The magenta crosses on the isobaths mark the zonal limits of the segments whose names are indicated in red text. The model control volume for a number of calculations described in the text is delimited by the 800 and 2500 m isobaths. A-B = Amundsen–Bellingshausen, WAP = Western Antarctic Peninsula, W-EA = Western East Antarctica, and E-EA = Eastern East Antarctica.

The vortex stretching, lateral viscous torque and nonlinear torque have the smallest spatial scales and are qualitatively similar, suggesting a two- or three-way balance at leading order.

The top panel of Fig. 4 shows the 2005–09 averages of the terms in Eq. (2), area-averaged within the circumpolar control volume delimited by the 800 and 2500 m isobaths (Fig. 1). ERRCOR and PGRD_ξ are omitted, as they are at least two orders of magnitude smaller than the other terms (Fig. 3). The leading-order balance in the circumpolar average is between the lateral viscous torque HVIS_ξ and the bottom vortex stretching $-fw_I$. The nonlinear torque, the vertical frictional torque, and the $-\beta V$ terms are smaller in magnitude and comparable among themselves. However, the spatial averages taken over some of the segments are found to deviate from this circumpolar average pattern (Fig. 4, bottom three rows). For instance, the magnitude of the nonlinear term is largest in the WAP, Weddell, Ross, and W-EA segments, suggesting that eddies or interactions between topography and slope currents may be playing a more important role there than in the other three segments. The $-fw_I$ and nonlinear terms have the same sign in the W-EA segment and seem to balance HVIS_ξ. The negative sign of the VVIS_ξ term (except in the WAP and W-EA segments) reflects the spatially broad cyclonic vorticity imparted at the surface by the wind and the sea ice year-round (Fig. 2 and left column of Fig. 5). It is also interesting to note that in the Amundsen–Bellingshausen, Weddell and E-EA segments the $-fw_I$ term is positive and the VVIS_ξ term is negative, which is qualitatively consistent with an upward surface Ekman velocity being equilibrated by an upward near-bottom velocity (due perhaps to upslope motion). The time-averaged residual term, containing the relative vorticity tendency ζ_t, is negligible in all segments in the 2005–09 average.

The ubiquity and persistence of the cyclonic vorticity forcing at the surface seen in Fig. 2 prompts an investigation of the seasonal variability of the water column. Figure 5 shows seasonal averages for the Amundsen–Bellingshausen segment of the net vertical frictional torque VVIS_ξ and the sum $\mathrm{stretch}_{\mathrm{res}} \equiv -fw_I + \mathrm{HVIS}_\xi - \mathrm{NONL}_\xi - \mathrm{RES}_\xi$. We interpret $\mathrm{stretch}_{\mathrm{res}}$ as the portion

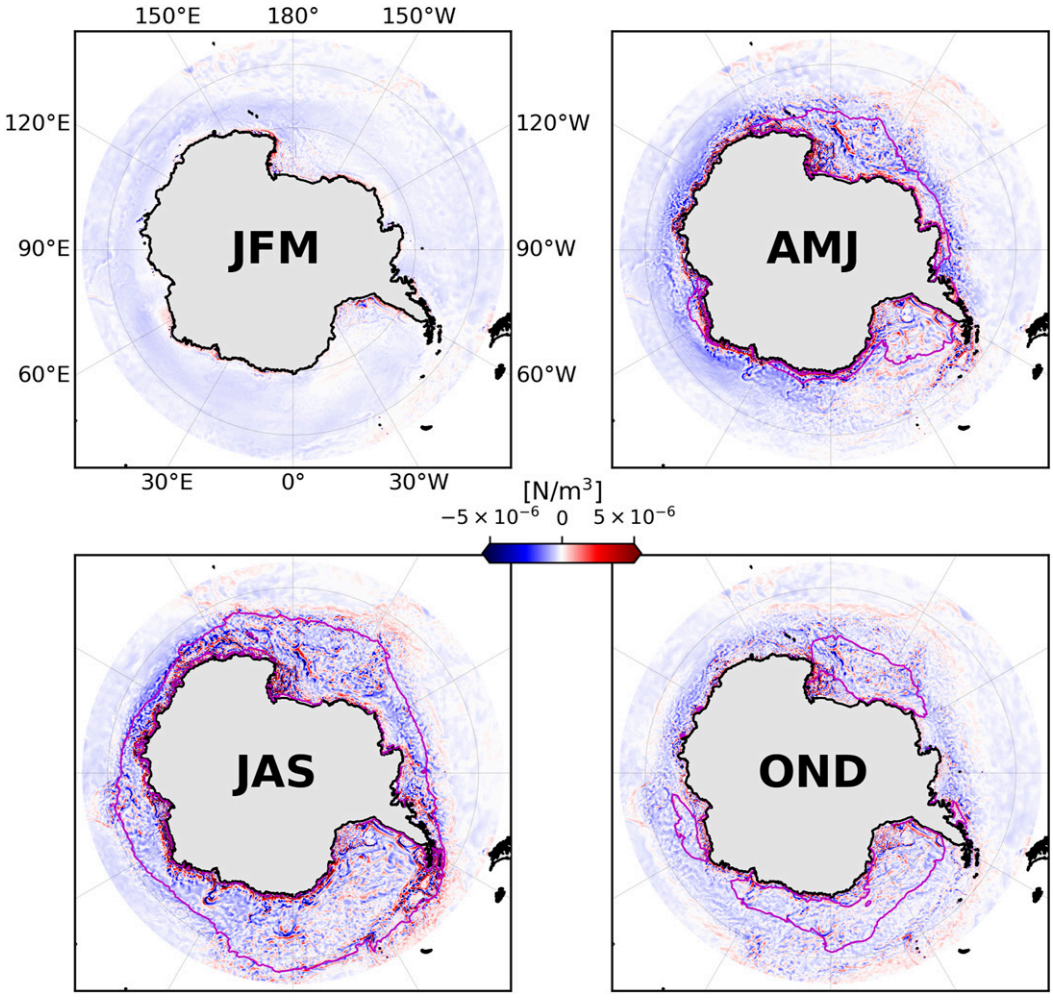

FIG. 2. Seasonal variability of the time-averaged (2005–09) total (wind + sea ice) surface stress curl (color shading) and sea ice edge (magenta line), defined as the 85% sea ice concentration contour. JFM, AMJ, JAS, and OND indicate austral summer, autumn, winter, and spring, respectively. Note that the surface stress curl is persistently cyclonic, suggesting an upward Ekman velocity and associated southward large-scale flow via conservation of planetary potential vorticity if a classic Sverdrup balance [SB in Eq. (1)] were to hold.

of the bottom vortex stretching term that does not balance the combination of the other three terms (the lateral frictional torque, the nonlinear torque and the vorticity tendency), and may therefore be balancing the net vertical frictional torque. As Fig. 2 suggests, the surface stress curl is mostly negative, especially in summer, under ice-free conditions (cf. Figs. 2, 5). The Antarctic Coastal Current is seen flowing westward, potentially contributing to the net vertical stress curl VVIS_{ξ}. The year-round similarity between the spatial structures of VVIS_{ξ} and $\mathrm{stretch}_{\mathrm{res}}$ is apparent in Fig. 5, which is physically consistent with the interpretation that part of the frictional torque that is introduced in the system forces meridional motion via conservation of planetary potential vorticity, and that part of this transport is blocked by the motion normal to the topography (see section 5 and Fig. 10).

4. The time–varying vorticity budget and TSB residual

Based on the description of the time-mean vorticity budget presented in the previous section and in agreement with the results of Hughes and de Cuevas (2001) and Wunsch (2011), it is clear that a classic Sverdrup balance is not a good model for the ACM, and that other terms in Eq. (1) must be considered to balance the cyclonic surface stress forcing. We thus investigate whether the TSB or the tTSB are valid diagnostic frameworks for the cross-slope flow in the ACM. We pursue this with correlation and

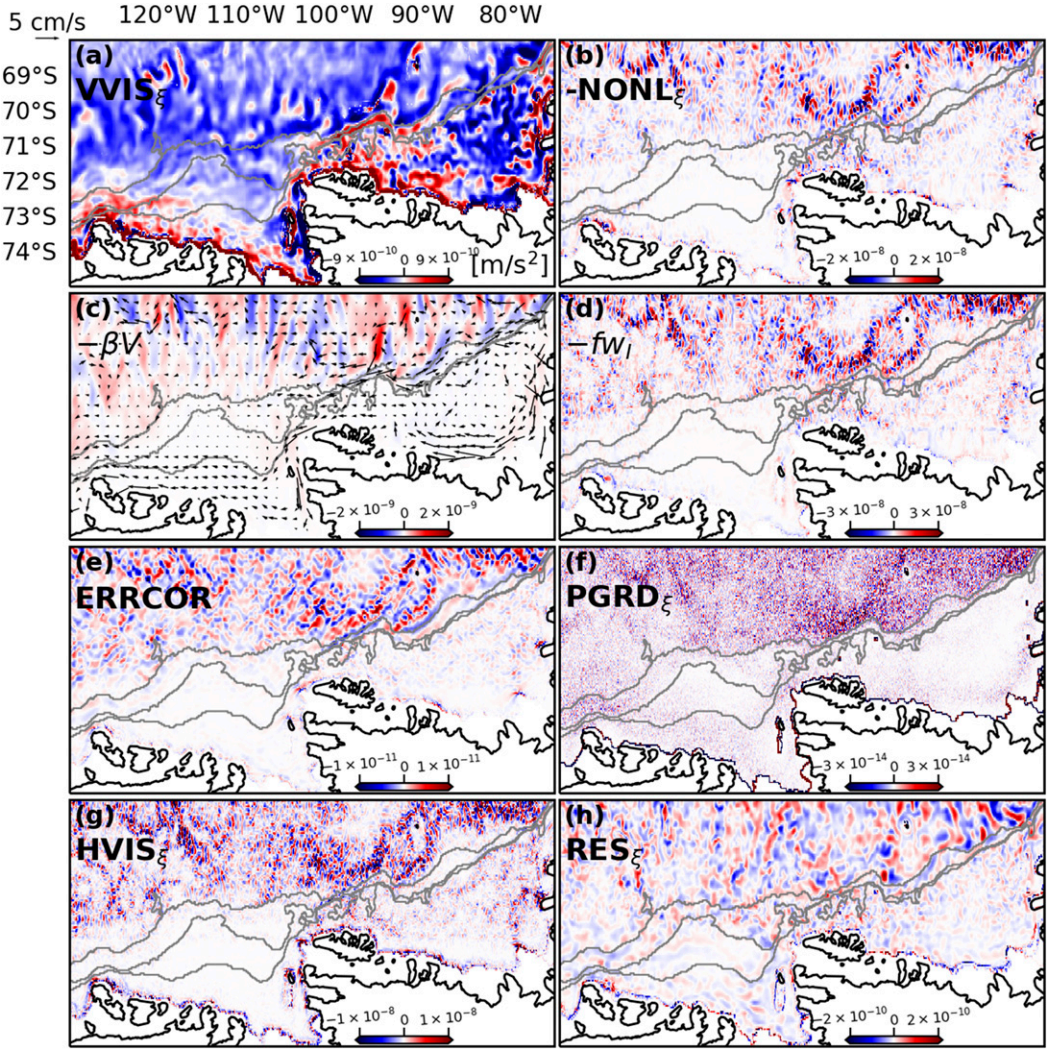

FIG. 3. Maps of the 2005–09 average of vertically integrated vorticity budget terms [Eq. (2)] in the Amundsen–Bellingshausen segment. (a) Net vertical frictional torque, VVIS$_\xi$; (b) nonlinear term, −NONL$_\xi$; (c) planetary vorticity advection, $-\beta V$; (d) bottom vortex stretching, $-fw_I$; (e) Coriolis error term, ERRCOR; (f) curl of the pressure gradient force, PGRD$_\xi$; (g) lateral frictional torque, HVIS$_\xi$; and (h) residual (truncation error + relative vorticity tendency), RES$_\xi$. The black arrows in (c) are the depth-averaged velocity field, and the gray lines are the 800, 1000, and 2500 m isobaths. Note the difference in the color scales.

coherence analyses between the time series of a subset of the vorticity terms in Eq. (2) averaged within the 800 and 2500 m isobaths in each of the six segments (Fig. 1) and over the full extent of the ACM.

a. Forcing-response correlations

The top panel of Fig. 6 shows the time series of the area averages of the vorticity terms over the entire continental slope. Consistent with the time-averaged fields in Fig. 5, VVIS$_\xi$ is mostly negative, and is balanced by the sum $-fw_I$ + HVIS$_\xi$ − NONL$_\xi$ − RES$_\xi$. The βV term is almost always positive (except for episodic reversals in the A-B, W-EA, and Ross segments) and one order of magnitude smaller than the others, indicating that, most of the time, the TSB acts to produce a net northward, offshore transport. The same cancellation between VVIS$_\xi$ and the four large terms is seen in all segments (Fig. 6, bottom three rows). An annual cycle is most evident in the W-EA segment, although it appears to exist in the other segments as well. An estimate of the segment-integrated meridional transport associated with the βV term is given in Fig. 6 for the A-B, Ross, W-EA, and E-EA segments. Caution is required in interpreting these estimates however, as they are $O(10)$ Sv and do not isolate the cross-isobath transport, but are instead a combination

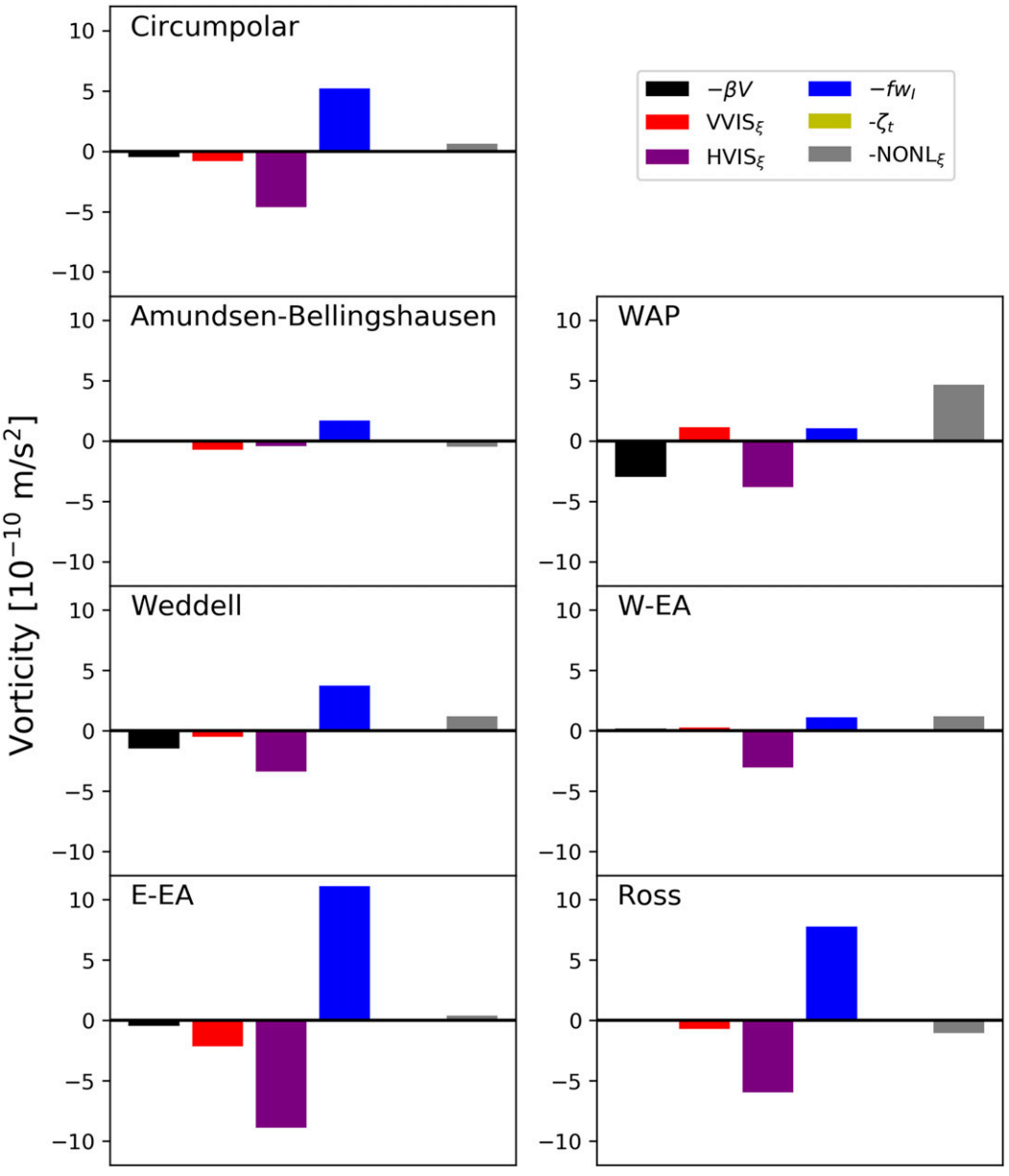

FIG. 4. The 2005–09 average of vertically integrated vorticity budget terms averaged over the strip bounded by the 800 and 2500 m isobaths. The top panel shows the circumpolar average, and other panels show averages taken over segments of the circumpolar strip.

of cross-isobath and along-isobath transports (see discussion in section 5).

At this point, we have established that the spatial and temporal variability of the vorticity budget is, to leading order, a cancellation of large terms (primarily $-fw_I$ and HVIS$_\xi$, Figs. 4–6). We are now in a position to test the hypothesized vorticity balances (TSB and tTSB). The reason why we do not include HVIS$_\xi$ in the balances is that $-fw_I$ and HVIS$_\xi$ do not fully cancel out everywhere, but rather, $-fw_I$ tends to be slightly larger or much larger than HVIS$_\xi$, leaving a residual that may be balanced by other terms (Fig. 4). However, the confirmation of this conjecture requires a correlation analysis, which will be presented next.

We begin by defining the forcing $F \equiv \text{VVIS}_\xi$ and the response $R_1 \equiv \beta V + fw_I$ (for the TSB) or $R_2 \equiv \beta V + fw_I + \text{RES}_\xi$ (for the tTSB), where the $-\beta V$ and $-fw_I$ terms are now grouped on the left-hand side of Eq. (2) and have therefore switched signs. We plot their time series in Fig. 7. In both the TSB and tTSB

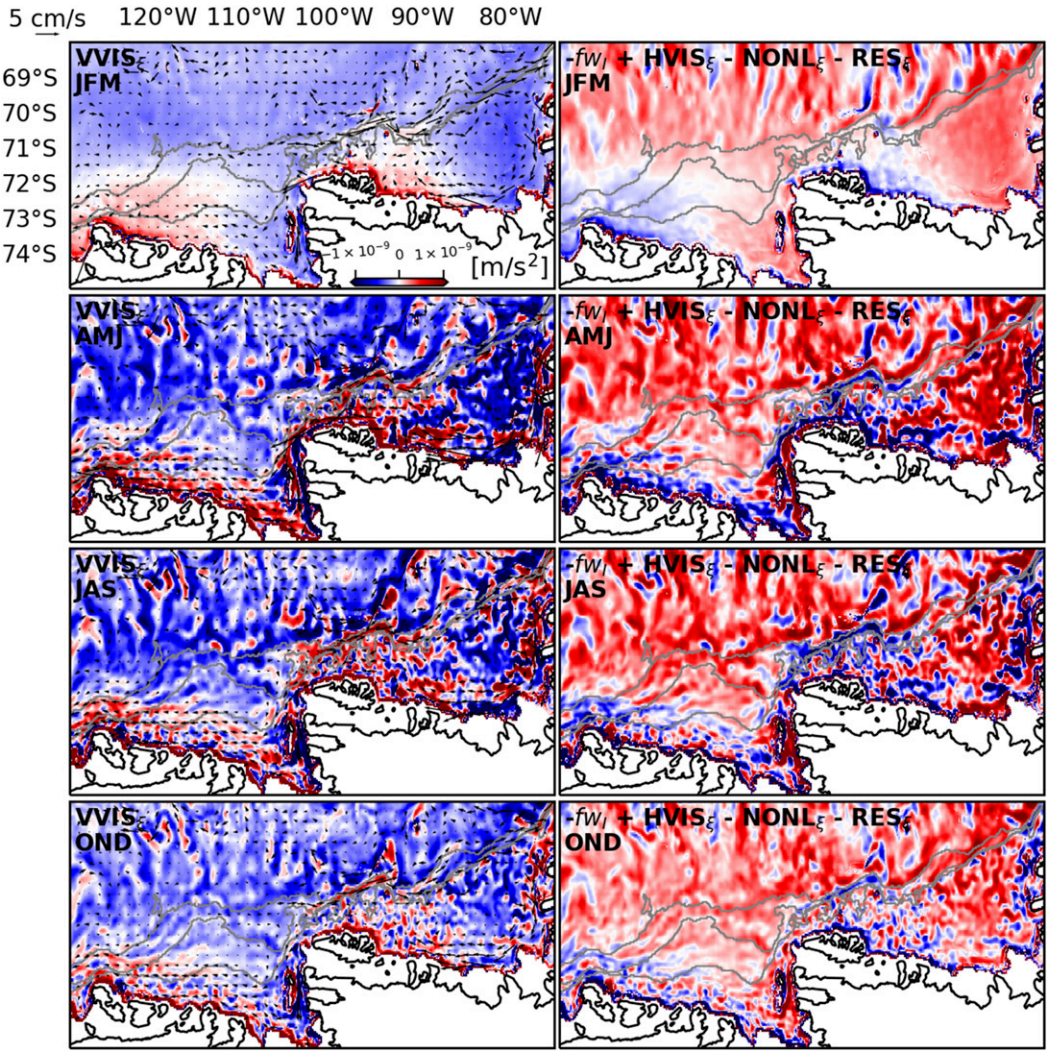

FIG. 5. Maps of the 2005–09 seasonal averages (from top to bottom: JFM, AMJ, JAS, and OND) of (left) the vertical frictional torque term, VVIS_ξ, and (right) the bottom vortex stretching residual, $-fw_I + \mathrm{HVIS}_\xi - \mathrm{NONL}_\xi - \mathrm{RES}_\xi$, in the Amundsen–Bellingshausen segment. The gray lines are the 800, 1000, and 2500 m isobaths. The black arrows in the left column are the depth-averaged velocity field. The color scale is the same for all panels.

cases, the response tracks the forcing for most of the time series, with some departures in the latter halves of 2006, 2007, and 2008. Regionally, the TSB seems to be a good approximation for the Amundsen–Bellingshausen, Weddell and W-EA segments (Fig. 7, bottom three rows). The episodic departures seen in the tTSB for the circumpolar average (Fig. 7, top panel) are most evident in the W-EA and E-EA segments.

The time series presentation is useful to reveal persistent correlations between the forcing (F) and different responses (R_1 and R_2); however, it is based on spatial averages. We therefore examine the spatial extent of these correlations. Figure 8 shows the 2005–09 mean geographic distribution of the TSB residual, defined as

$$\mathrm{TSB}_{\mathrm{res}} \equiv F - R_1 = \mathrm{VVIS}_\xi - \beta V - fw_I. \qquad (3)$$

It can be seen that the WAP and the East Antarctica segments have relatively larger residuals, while areas of relatively smaller $\mathrm{TSB}_{\mathrm{res}}$ are found in the Amundsen and Weddell Seas, and to a lesser extent, in the Ross Sea. The areas of local spatial minima of $\mathrm{TSB}_{\mathrm{res}}$ extend over large spans of the ACM, notably over the entire broad continental shelves of the Amundsen and Weddell Seas.

Even in the regions of local minima found in Fig. 8, the $\mathrm{TSB}_{\mathrm{res}}$ is often of the same size as the other terms in the

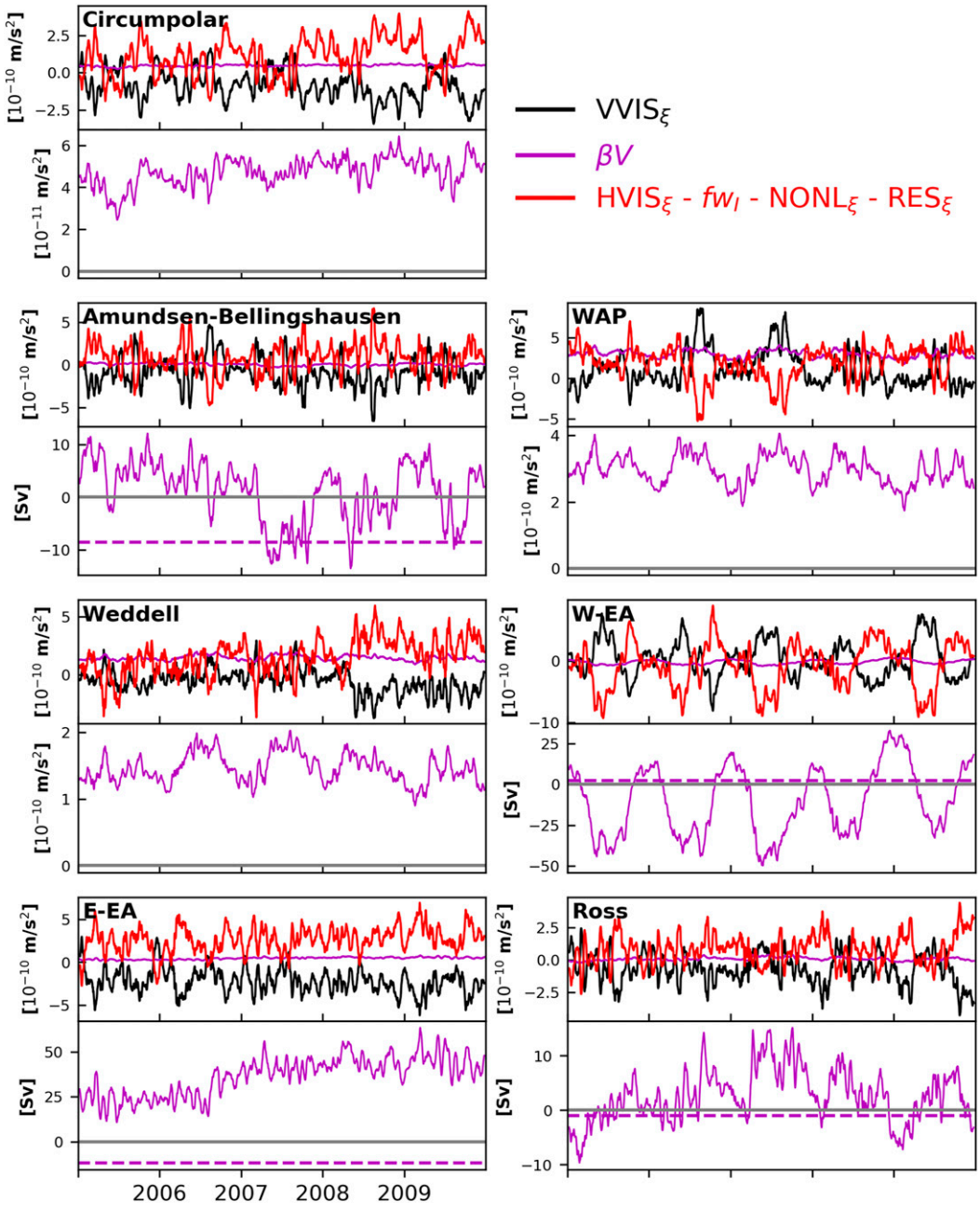

FIG. 6. Balance of leading-order terms in the area-averaged vorticity budget. The top subpanels show VVIS_ξ (forcing), $\mathrm{HVIS}_\xi - fw_I - \mathrm{NONL}_\xi - \mathrm{RES}_\xi$ (bottom vortex stretching residual), and βV. The bottom subpanels show only the βV term. The βV term is a small residual of the cancellation of large terms. The top-left panel shows the circumpolar average, and the other panels show averages taken over segments of the circumpolar strip. For segments with a predominant zonal orientation (A-B, W-EA, E-EA, and Ross, see Fig. 1), βV is given in units of volume transport (i.e., βV multiplied by L/β, where L is the length of the 800 m isobath in the segment) in the lower subpanels. The horizontal magenta lines indicate the transport values estimated in Table 2. All time series were smoothed with a 15-day running mean window. Note the different y scales.

vorticity budget. So are F and R_1 or R_2 quantitatively correlated? Table 1 shows the zero-lag correlation coefficients for the two hypothesized balances (TSB and tTSB), where the estimate of effective degrees of freedom for the minimum significant correlation coefficient was calculated based on an integral time scale of 5 days, computed as the maximum between the integral time scales of either the F and R_1 or F and R_2. One might

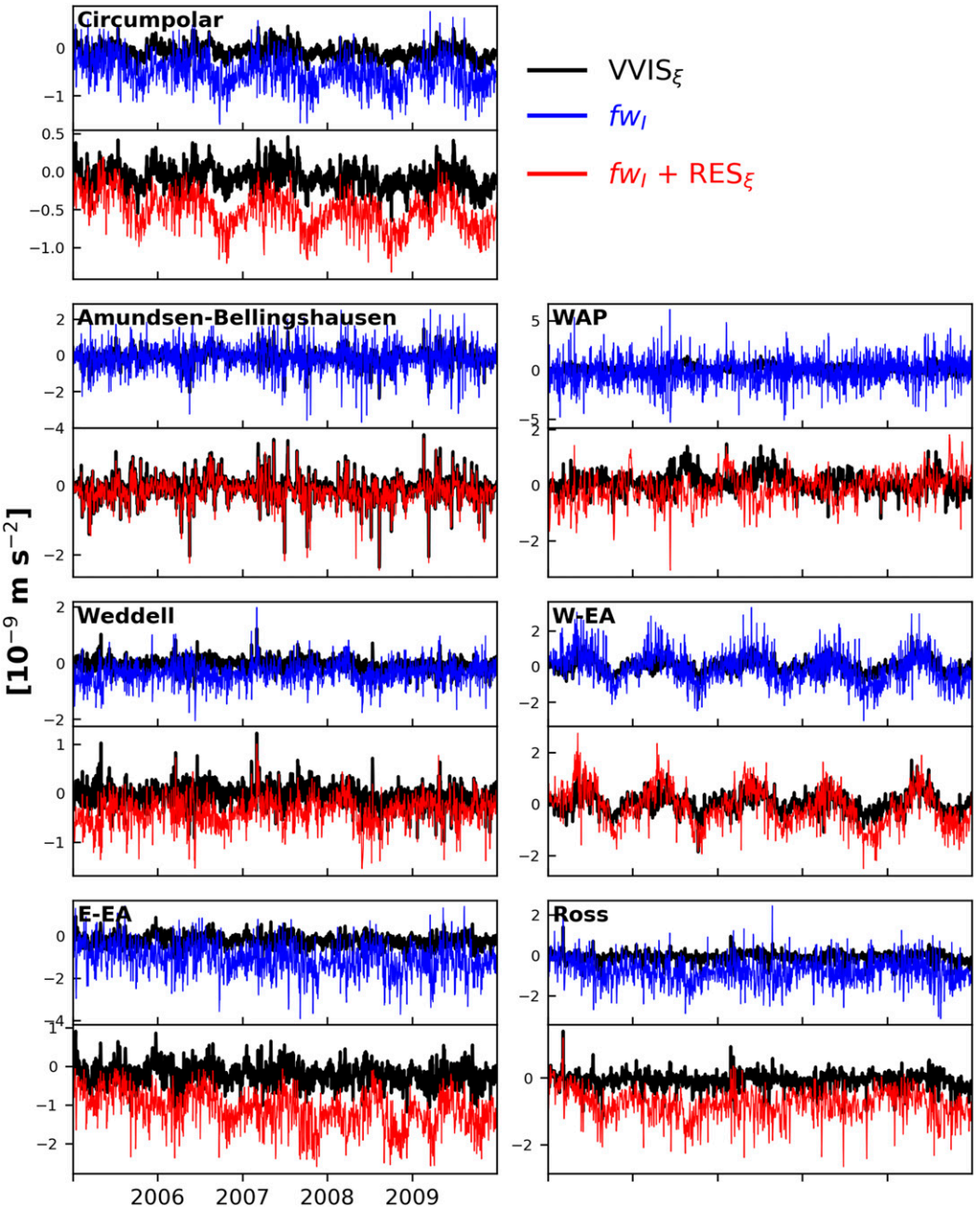

FIG. 7. Time series of the forcing term $F = \text{VVIS}_\xi$ and two simplified vorticity balances assumed as a response term R for the area-averaged budget. Top subpanels show TSB ($R_1 = \beta V + fw_I$) and bottom subpanels show tTSB ($R_2 = \beta V + fw_I + \text{RES}_\xi$). The top-left panel shows circumpolar average, and the other panels show averages taken over segments of the circumpolar strip. The βV term is smaller and has been omitted for simplicity.

expect the correlations to be maximum at nonzero lags due to frictional effects (Gille et al. 2001). However, the correlations are all maximum at zero lag or lags of few days (not shown). This result suggests that F and either R_1 or R_2 generally balance directly. Intuitively, correlations are highest for the tTSB (i.e., F with R_2 rather than F with R_1) in all segments (except for the WAP segment). Consistent with the spatial patterns seen in Fig. 8, the highest-correlation segment for TSB is the Amundsen–Bellingshausen.

b. Forcing-response coherence spectra

While tTSB appears to offer a better representation than TSB of the dominant dynamics, there is no guarantee

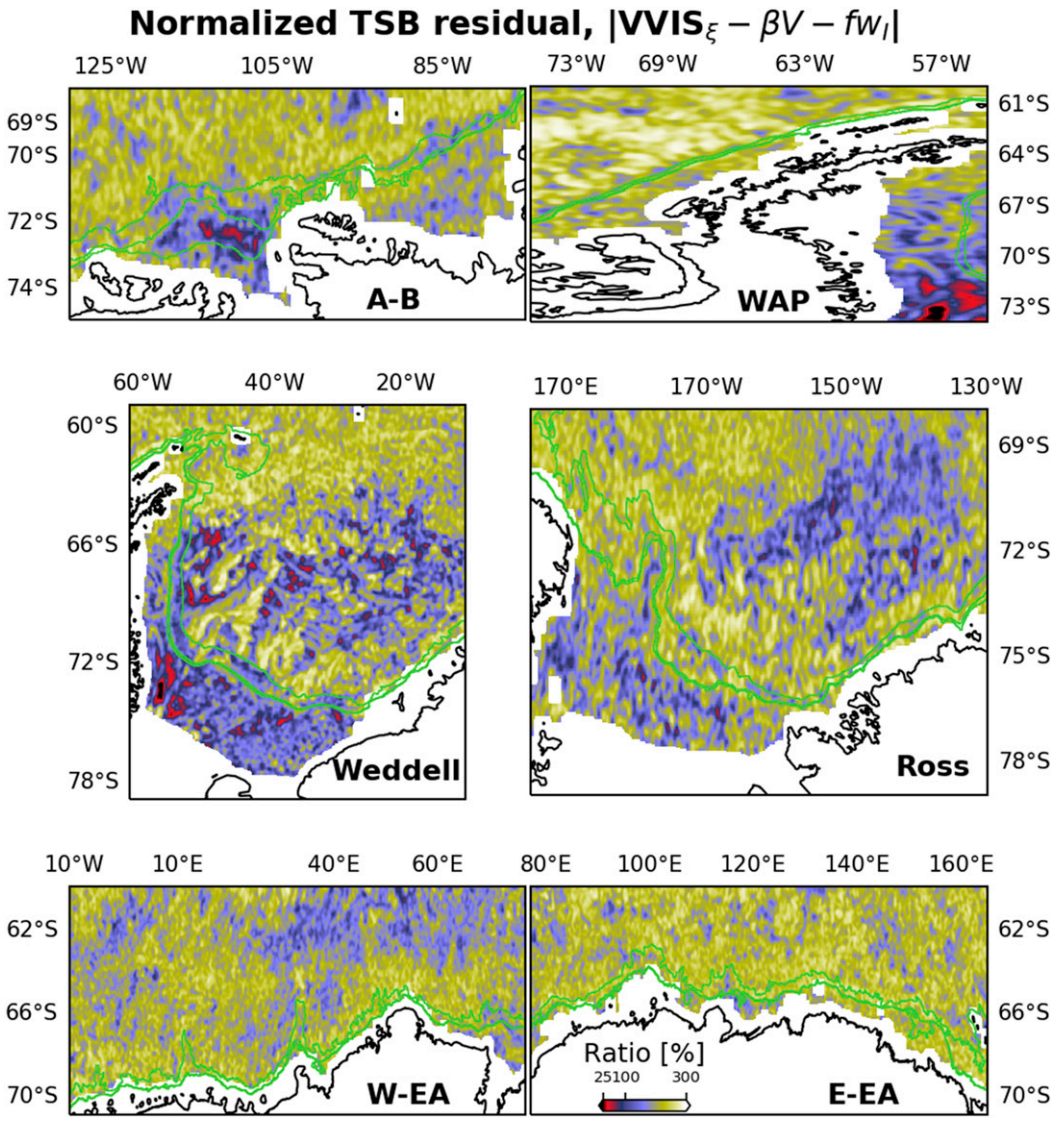

FIG. 8. Maps of the 2005–09 average of the residual of the TSB, $R_{Sv} \equiv \text{VVIS}_\xi - \beta V - fw_I$ for each of the six segments. The green lines are the 800, 1000, and 2500 m isobaths. The color scale is the same for all panels and indicates the ratio of the absolute value of R_{Sv} to the mean of the absolute values of all terms, at each grid cell. The fields have been smoothed with a two-dimensional Gaussian filter.

that this is true over all time scales. We use coherence analysis between the time series of F and either R_1 or R_2 (Fig. 9) to assess the frequency dependence of the balance. In agreement with Table 1, the tTSB holds well for all segments at high frequencies (with the exception of the WAP segment), with squared coherences nearing 1. The higher coherences for the TSB at low frequencies in the Amundsen–Bellingshausen lends

TABLE 1. Zero-lag correlation coefficients (columns) between forcing (F) and response (R_1 or R_2) functions; $F = \text{VVIS}_\xi$ for both rows, $R_1 = \beta V + fw_I$ for the TSB, and $R_2 = \beta V + fw_I + \text{RES}_\xi$ for the tTSB. The minimum statistically significant correlation coefficient at the 99% confidence level is 0.14, assuming a conservative integral time scale of 5 days for F, R_1, and R_2.

	A-B	WAP	Weddell	W-EA	E-EA	Ross	Circumpolar average
TSB	0.54	0.18	0.36	0.36	0.26	0.19	0.40
tTSB	0.94	0.11	0.74	0.52	0.63	0.48	0.61

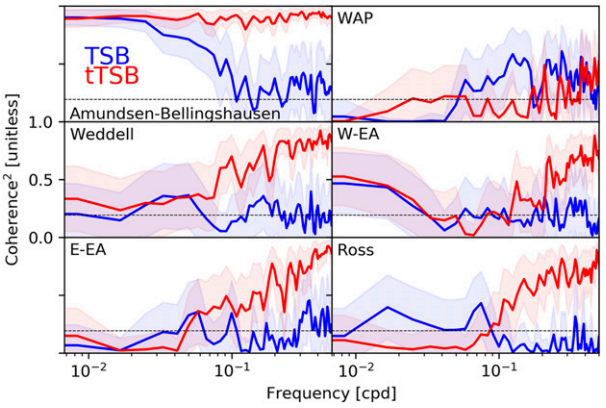

FIG. 9. Coherence amplitude spectra between forcing $F \equiv \mathrm{VVIS}_\xi$ and response R functions, estimated with 80 degrees of freedom. For the TSB time series (blue lines), $R_1 \equiv \beta V + fw_I$. For the tTSB time series (red lines), $R_2 \equiv \beta V + fw_I + \mathrm{RES}_\xi$. The shading indicates the 95% confidence intervals of the coherence estimates. The dashed lines are the level of no significance at the 95% confidence level.

further support to the results of the correlation analyses (Table 1) and to the spatial minimum in the residual of the TSB (Fig. 8). The W-EA segment also displays relatively high coherences for the TSB at low frequencies, although Fig. 8 shows no conspicuous local minima in $\mathrm{TSB}_{\mathrm{res}}$ there, meaning that the terms have substantial covariance despite having a large mean residual. The tTSB holds exceptionally well for the Amundsen–Bellingshausen segment at all frequencies, while it is marginally significant at low frequencies in the Weddell segment.

5. Discussion and conclusions

We have diagnosed the circumpolar-averaged and regional vorticity budgets in a global, eddy-permitting ocean/sea ice simulation and have shown that, in some regions of the Antarctic continental margin (ACM), the flow follows a simplified transient Sverdrup-like balance [tTSB, Eq. (1)]. The Amundsen and Weddell Seas (and to a lesser extent, the W-EA segment) emerge as regions where an even simpler, steady, TSB [Eq. (1)] is found in the 2005–09 average. Figure 10 gives a physical interpretation of these two diagnostic results. In the TSB, there is a steady-state equilibration between the surface vortex stretching/squashing imparted by the surface Ekman pumping and the bottom vortex squashing/stretching imparted by cross-slope motion. In the tTSB, relative vorticity fluctuations are important and can be understood as the manifestation of forced topographically trapped waves, which displace water columns up- and downslope while propagating westward.

Quantitatively, how important is the TSB for the cross-slope transport of volume and heat? We present in Table 2 rough estimates for the approximately zonally oriented segments (A-B, W-EA, E-EA, and Ross) based on the time-averaged (2005–09) forcing $F \equiv \mathrm{VVIS}_\xi$ scaled by $r^2 L/\beta$, where r is the TSB forcing-response correlation coefficient (Table 1) and L is the length of the segment. The rationale for this estimate is that each term in Eqs. (1) and (2) may be interpreted as a meridional transport per unit length (if these equations are divided through by β), and therefore the fraction of $R_1/\beta = V + fw_I/\beta$ that covaries with the forcing VVIS/β (this fraction is obtained by scaling VVIS/β by r^2) is an estimate of the net meridional transport associated with the two response terms in the TSB. The associated heat transports are obtained by multiplying the volume transports by $\rho C_p \Delta T$ where $\rho = 1027\,\mathrm{kg\,m^{-3}}$ is the density, $C_p = 4000\,\mathrm{J\,kg^{-1}\,K^{-1}}$ is the specific heat capacity and $\Delta T = 0.5\,\mathrm{K}$ is an approximate estimate of the temperature of seawater above the freezing point. The A-B and E-EA are the segments with the largest onshore TSB-related volume and heat transports, while the Ross and W-EA have smaller transports. Note that the heat transports may be larger in segments where warmer branches of CDW (larger ΔT) are present on the continental slope.

We emphasize that caution is required in interpreting the transport estimates in Table 2, as well as those in Fig. 6. The $O(10)$ Sv total transport derived from the βV term (Fig. 6) is much larger than the $O(0.1)$ Sv estimates of the cross-slope overturning circulation, either in the geostrophic interior or in the surface and bottom Ekman layers (e.g., Wåhlin et al. 2012; Stewart and Thompson 2015; Palóczy et al. 2018). Since it is the meridional transport (not the cross-isobath transport) that appears in the vorticity equation [Eqs. (1) and (2)], and the ACM is not perfectly zonally oriented (Figs. 1, 8), one should not expect the TSB and the tTSB to isolate only the cross-isobath transport, hence leading to the discrepancy between the transport estimates in Fig. 6 and Table 2. We hypothesize that our vorticity-based dynamical argument can explain only a fraction of the onshore or offshore transport, and that this fraction varies regionally along the ACM.

The potential implications of these dynamics are greatest for the Amundsen Sea, where warm Circumpolar Deep Water has access to the ice shelves that buttress most of the West Antarctic Ice Sheet (e.g., Schmidtko et al. 2014; Silvano et al. 2016). We note that measurements have shown that the surface stress curl (from wind and sea ice) at the shelf break correlates with bottom temperature in Dotson Trough, located in the central Amundsen Sea (Kim et al. 2017). This provides

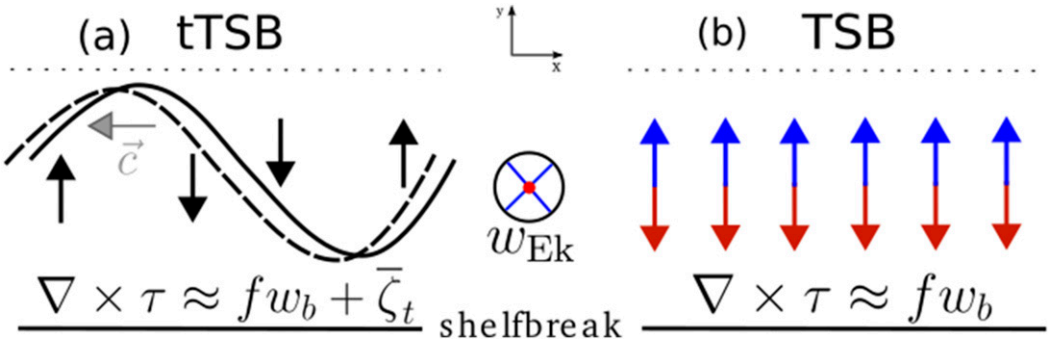

FIG. 10. Cartoon illustrating a physical interpretation of the cross-slope transport in (a) the tTSB and (b) the steady TSB over a zonally oriented continental margin. The βV term has been omitted for simplicity because it is usually an order of magnitude smaller than the other terms (Fig. 6). Here, $\boldsymbol{\tau} \equiv \boldsymbol{\tau}_s - \boldsymbol{\tau}_b$ is the net kinematic stress vector, and other terms follow Eq. (1). In (a), the gray arrow indicates the direction of propagation of the topographically trapped waves associated with the tTSB, and the black arrows indicate the associated instantaneous meridional, cross-slope flow. The black curves illustrate the displacement of a waveform (from solid to dashed). In (b), the red arrows indicate onshore transport associated with upward Ekman pumping ($w_{\mathrm{EK}} > 0$, directed out of the page), while the blue arrows indicate offshore transport associated with downward Ekman pumping ($w_{\mathrm{EK}} < 0$, directed into the page).

observational support for our hypothesis that the surface stress curl might play an important role in the cross-isobath transport of heat (both onshore and offshore) via a Sverdrup-like vorticity balance, and it also agrees with Rodriguez et al.'s (2016) model results where a net onshore transport linked to the wind stress curl was found.

Dotto et al. (2019) have shown the importance of two different mechanisms in different regions of the Amundsen Sea. The first one is change in water mass properties (along the same isopycnal) entering the continental shelf, and the second one is isopycnal heaving without change in the water mass properties. They related the variations in the water mass properties to wind-driven variations in the speed of an eastward undercurrent on the continental slope (a baroclinic feature also observed by Walker et al. 2013), and interpreted the isopycnal heaving as due to locally induced vertical velocities associated with Ekman pumping. We argue that the TSB mechanism discussed in this study may play a role in these processes by meridionally transporting different water mass classes toward or away from the slope undercurrent in the water mass property change mechanism, and by locally inducing meridional transport associated with the isopycnal heaving mechanism (due to conservation of planetary potential vorticity).

In analyses of the depth-integrated vorticity budget in global models, areas with smoother bottom topography in the interior of tropical and subtropical basins have been found to be closer to classic Sverdrup balance [$\beta V \approx \nabla \times \boldsymbol{\tau}_s$ in Eq. (1); see Wunsch 2011], while the rough Southern Ocean and steep continental margins have been dominated by bottom pressure torques (Hughes and de Cuevas 2001; Lu and Stammer 2004; Yeager 2013, 2015). The fact that the influence of remote wind perturbations communicated via barotropic Kelvin waves have been suggested to be strongest in steep regions like the WAP (Spence et al. 2017; Webb et al. 2019) is consistent with the fact that this segment has the poorest correlations and coherence magnitudes for the tTSB (Table 1, Figs. 7, 9), and has also the narrowest and steepest continental slope (Fig. 1). A physical interpretation of this is that relative vorticity fluctuations in the WAP are not being forced by the local surface stress curl as in a tTSB (Fig. 10a), but rather by remotely generated topographically trapped waves propagating through the region, or by nonlinear effects associated with the impingement of offshore currents. We also note that in an eddy-permitting simulation such as the one we consider here, nontopographic effects such as convergence of eddy vorticity fluxes (e.g., Williams et al. 2007; Delman et al. 2015) are likely to play a role, although such effects are beyond the scope of our study. Eddy vorticity forcing in the ACC and ASC might help

TABLE 2. Rough estimates of volume and heat transports associated with the TSB. The volume transports are obtained by multiplying the time-averaged forcing (VVIS_{ξ}) by $r^2 L/\beta$, where r is the TSB correlation coefficient (Table 1) and L is the length of the segment. The heat transports are obtained by multiplying the volume transports by $\rho C_p \Delta T$, where ρ, C_p, and ΔT are typical values for the density, the specific heat capacity, and the temperature above the freezing point, respectively.

	A-B	W-EA	E-EA	Ross
TSB volume transport (Sv)	−8.5	2.1	−11.8	−1.0
TSB heat transport (TW)	−17.4	4.2	−24.3	−2.0

explain the large vertical velocities in the W-EA and E-EA segments (not shown).

The picture discussed in this study is likely robust at large scales and low frequencies. However, we remind the reader of the limitations of our analyses. The model resolution is not sufficient to fully resolve eddies in the ACM (Stewart and Thompson 2015), and the lack of ice shelf cavities, tides, and realistic continental freshwater sources also limits the realism of the simulation, especially on the continental shelf. The lack of tidal momentum flux convergences around the shelf break is expected to impact the structure of the ASC (Flexas et al. 2015; Stewart et al. 2019), which might modify the cross-slope transport of heat and other properties at tidal and supertidal frequencies (Stewart et al. 2018, 2019).

An interesting and important related question that could be addressed in future work is whether averaging the vorticity balance over even longer time scales would expand the areas over which the depth-integrated flow is in approximate TSB. A similar question was asked by Wunsch (2011) for the classic Sverdrup balance based on the analysis of a 16-yr average global state estimate. We are limited by the five years (2005–09) over which model output necessary to close the vorticity budget is available, although it may be possible to test correlations between approximations to the vorticity budget terms reconstructed from the velocity and surface stress curl fields in the monthly averaged output of the simulation.

In summary, we have presented evidence for the existence of an approximate topographic Sverdrup balance in some areas of the ACM in a global eddy-permitting simulation. Because sea ice extent and winds change unevenly in the Southern Ocean, sectors of the ACM are expected to be exposed in different ways to low-frequency wind- and ice-stress curl. For example, the effects of poleward shifting easterlies on the heat content of the Antarctic continental shelf, as studied in global climate models by Spence et al. (2014, 2017), Goddard et al. (2017), Palóczy et al. (2018), Webb et al. (2019), and others, might be expected to affect the cross-slope transport of heat in the Amundsen, Bellingshausen, and Weddell Seas and in parts of East Antarctica more strongly than elsewhere in the ACM.

Acknowledgments. A.P., J.L.M, and S.T.G. gratefully acknowledge support from the U.S. Department of Energy (DOE, Grants DE-SC0014440 and DE-SC0020073) and high-performance computing support from Yellowstone (ark:/85065/d7wd3xhc) provided by NCAR's Climate Simulation Laboratory (CSL), sponsored by the National Science Foundation (NSF) and other agencies. J.L.M. was supported by an earlier U.S. DOE Office of Science grant entitled "Ultra-High Resolution Global Climate Simulation" via a Los Alamos National Laboratory subcontract to carry out the POP/CICE simulation; both Caroline Papadopoulos (SIO/UCSD) and Elena Yulaeva (UCSD) participated in its production. S.T.G. also acknowledges NSF Awards PLR-1425989 and OCE 1658001. The analyses of the model output performed in this study were enabled by computing resources provided by Oak Ridge Leadership Computing Facility (OLCF). We are also grateful to Andrew Stewart (University of California, Los Angeles) and Matt Mazloff (SIO/UCSD), for insightful exchanges and Steve Yeager (National Center for Atmospheric Research) for the additional POP code needed to archive non-standard terms for the budget as well as an NCAR Command Language (NCL) vorticity budget code that provided a starting place for our expanded Fortran-based budget code used in this study. Thoughtful critiques and comments from two anonymous reviewers substantially improved the quality of the manuscript. Reduced datasets and code necessary to reproduce the results are available at https://github.com/apaloczy/AntarcticaVorticityBudget.

APPENDIX

Discretization of the Depth-Integrated Vorticity Equation

To arrive at the discrete form of the depth-integrated vorticity equation [Eq. (2)], we begin with the continuous depth-dependent momentum equation,

$$\mathbf{u}_t + \mathbf{u}\cdot\nabla\mathbf{u} + \mathbf{f}\times\mathbf{u} = -\nabla p + A_H\nabla^4\mathbf{u} + (A_v\mathbf{u}_z)_z, \quad \text{(A1)}$$

where $\mathbf{f}\equiv\hat{\mathbf{z}}f$, p is pressure, A_v is the vertical viscosity coefficient, and ∇^4 is the horizontal biharmonic operator. Taking the discrete curl of (A1) gives

$$\zeta_t + \nabla\times(\mathbf{u}\cdot\nabla\mathbf{u}) + \nabla\times(\mathbf{f}\times\mathbf{u}) = -\nabla\times(\nabla p) + A_H\nabla^4\zeta + \nabla\times[(A_v\mathbf{u}_z)_z], \quad \text{(A2)}$$

where the curl of the pressure gradient term vanishes at interior grid cells only in the case of uniform grid spacing (Bell 1999, although we find it to be negligible, Fig. 3f), but is large at grid cells with sidewalls (Yeager 2013), which we do not include in the vertical integrals. Applying the discrete curl operator to the Coriolis term on a B grid gives

$$\nabla\times(\mathbf{f}\times\mathbf{u}) = -fw_z + \beta v - \mathrm{ERRCOR}, \quad \text{(A3)}$$

where ERRCOR is a numerical artifact of the discretization (see Bell 1999; Yeager 2013, for details). Vertically integrating (A2) using (A3) gives

$$\partial_t \overline{\zeta} = -\beta\overline{v} + f[w(0) - w(z_I)] - \overline{\nabla \times (\mathbf{u} \cdot \nabla \mathbf{u})} - \overline{\nabla \times (\nabla p)} + \overline{A_H \nabla^4 \zeta} + \overline{\nabla \times [(A_v \mathbf{u}_z)_z]} + \overline{\mathrm{ERRCOR}}, \tag{A4}$$

where overbars indicate vertical integrals from $z = z_I$ to $z = 0$, and $z_I(x, y)$ is determined from the minimum of the vertical indices of the bottom cells of the four surrounding U points in the model's B grid, minus one vertical cell index. This places the lower limit of integration at a grid cell that has no sidewalls (Bell 1999). By approximating $w(z = 0) \approx 0$, defining $V \equiv \overline{v}$, $\overline{\mathrm{RES}_\xi} \equiv \partial_t \overline{\zeta}$, $\overline{\mathrm{NONL}_\xi} \equiv \overline{\nabla \times (\mathbf{u} \cdot \nabla \mathbf{u})}$, $\overline{\mathrm{PGRD}_\xi} \equiv -\overline{\nabla \times (\nabla p)}$, $\overline{\mathrm{HVIS}_\xi} \equiv \overline{A_H \nabla^4 \zeta}$, $\overline{\mathrm{VVIS}_\xi} \equiv \overline{\nabla \times [(A_v \mathbf{u}_z)_z]}$, $w(z_I) \equiv w_I$, absorbing the numerical truncation error into the residual term $\overline{\mathrm{RES}_\xi}$ and dropping overbars results in Eq. (2).

REFERENCES

Armitage, T. W. K., R. Kwok, A. F. Thompson, and G. Cunningham, 2018: Dynamic topography and sea level anomalies of the Southern Ocean: Variability and teleconnections. *J. Geophys. Res. Oceans*, **123**, 613–630, https://doi.org/10.1002/2017JC013534.

Bell, M. J., 1999: Vortex stretching and bottom torques in the Bryan-Cox ocean circulation model. *J. Geophys. Res. Oceans*, **104**, 23 545–23 563, https://doi.org/10.1029/1999JC900064.

Brink, K., 2016: Cross-shelf exchange. *Annu. Rev. Mar. Sci.*, **8**, 59–78, https://doi.org/10.1146/annurev-marine-010814-015717.

Castagno, P., P. Falco, M. S. Dinniman, G. Spezie, and G. Budillon, 2017: Temporal variability of the circumpolar deep water inflow onto the Ross Sea continental shelf. *J. Mar. Syst.*, **166**, 37–49, https://doi.org/10.1016/j.jmarsys.2016.05.006.

Delman, A. S., J. L. McClean, J. Sprintall, L. D. Talley, E. Yulaeva, and S. R. Jayne, 2015: Effects of eddy vorticity forcing on the mean state of the Kuroshio extension. *J. Phys. Oceanogr.*, **45**, 1356–1375, https://doi.org/10.1175/JPO-D-13-0259.1.

Depoorter, M. A., J. L. Bamber, J. A. Griggs, J. T. M. Lenaerts, S. R. M. Ligtenberg, M. R. van den Broeke, and G. Moholdt, 2013: Calving fluxes and basal melt rates of Antarctic ice shelves. *Nature*, **502**, 89–92, https://doi.org/10.1038/nature12567.

Dotto, T. S., and Coauthors, 2019: Wind-driven processes controlling oceanic heat delivery to the Amundsen Sea, Antarctica. *J. Phys. Oceanogr.*, **49**, 2829–2849, https://doi.org/10.1175/JPO-D-19-0064.1.

Flexas, M. M., M. P. Schodlok, L. Padman, D. Menemenlis, and A. H. Orsi, 2015: Role of tides on the formation of the Antarctic slope front at the Weddell-Scotia confluence. *J. Geophys. Res. Oceans*, **120**, 3658–3680, https://doi.org/10.1002/2014JC010372.

Gille, S. T., D. P. Stevens, R. T. Tokmakian, and K. J. Heywood, 2001: Antarctic Circumpolar Current response to zonally averaged winds. *J. Geophys. Res.*, **106**, 2743–2759, https://doi.org/10.1029/1999JC900333.

Goddard, P. B., C. O. Dufour, J. Yin, S. M. Griffies, and M. Winton, 2017: CO_2-induced ocean warming of the Antarctic Continental Shelf in an eddying global climate model. *J. Geophys. Res. Oceans*, **122**, 8079–8101, https://doi.org/10.1002/2017JC012849.

Holland, W. R., 1973: Baroclinic and topographic influences on the transport in western boundary currents. *Geophys. Fluid Dyn.*, **4**, 187–210, https://doi.org/10.1080/03091927208236095.

Holloway, G., 2008: Observing global ocean topostrophy. *J. Geophys. Res.*, **113**, C07054, https://doi.org/10.1029/2007JC004635.

Hughes, C. W., and B. A. de Cuevas, 2001: Why western boundary currents in realistic oceans are inviscid: A link between form stress and bottom pressure torques. *J. Phys. Oceanogr.*, **31**, 2871–2885, https://doi.org/10.1175/1520-0485(2001)031%3C2871:WWBCIR%3E2.0.CO;2.

Hunke, E. C., and W. H. Lipscomb, 2010: CICE: The Los Alamos Sea Ice Model documentation and software user's manual, version 4.1. Doc. LA-CC-06-012, 76 pp., http://csdms.colorado.edu/w/images/CICE_documentation_and_software_user's_manual.pdf.

Jacobs, S. S., A. Jenkins, C. F. Giulivi, and P. Dutrieux, 2011: Stronger ocean circulation and increased melting under Pine Island Glacier ice shelf. *Nat. Geosci.*, **4**, 519–523, https://doi.org/10.1038/ngeo1188.

Kim, T., H. Ha, A. Wåhlin, S. Lee, C. Kim, J. Lee, and Y. Cho, 2017: Is Ekman pumping responsible for the seasonal variation of warm circumpolar deep water in the Amundsen Sea? *Cont. Shelf Res.*, **132**, 38–48, https://doi.org/10.1016/j.csr.2016.09.005.

Large, W. G., and S. G. Yeager, 2009: The global climatology of an interannually varying air–sea flux data set. *Climate Dyn.*, **33**, 341–364, https://doi.org/10.1007/s00382-008-0441-3.

——, J. C. McWilliams, and S. C. Doney, 1994: Oceanic vertical mixing: A review and a model with a nonlocal boundary layer parameterization. *Rev. Geophys.*, **32**, 363–403, https://doi.org/10.1029/94RG01872.

Lu, Y., and D. Stammer, 2004: Vorticity balance in coarse-resolution global ocean simulations. *J. Phys. Oceanogr.*, **34**, 605–622, https://doi.org/10.1175/2504.1.

Mallett, H. K. W., L. Boehme, M. Fedak, K. J. Heywood, D. P. Stevens, and F. Roquet, 2018: Variation in the distribution and properties of circumpolar deep water in the eastern Amundsen Sea, on seasonal timescales, using seal-borne tags. *Geophys. Res. Lett.*, **45**, 4982–4990, https://doi.org/10.1029/2018GL077430.

McClean, J. L., and Coauthors, 2018: High-resolution fully-coupled ACME v0.1 approximate present day transient climate simulations. *2018 Ocean Sciences Meeting*, Portland, OR, Amer. Geophys. Union, Abstract OM44C-2143.

Mertz, G., and D. G. Wright, 1992: Interpretations of the JEBAR term. *J. Phys. Oceanogr.*, **22**, 301–305, https://doi.org/10.1175/1520-0485(1992)022<0301:IOTJT>2.0.CO;2.

Moffat, C., and M. Meredith, 2018: Shelf–ocean exchange and hydrography west of the Antarctic Peninsula: A review. *Philos. Trans. Roy. Soc.*, **A376**, 20170164, https://doi.org/10.1098/rsta.2017.0164.

Nøst, O. A., M. Biuw, V. Tverberg, C. Lydersen, T. Hattermann, Q. Zhou, L. H. Smedsrud, and K. M. Kovacs, 2011: Eddy overturning of the Antarctic Slope Front controls glacial melting in the Eastern Weddell Sea. *J. Geophys. Res.*, **116**, C11014, https://doi.org/10.1029/2011JC006965.

Palóczy, A., S. T. Gille, and J. L. McClean, 2018: Oceanic heat delivery to the Antarctic continental shelf: Large-scale, low-frequency variability. *J. Geophys. Res. Oceans*, **123**, 7678–7701, https://doi.org/10.1029/2018JC014345.

Rignot, E., S. Jacobs, J. Mouginot, and B. Scheuchl, 2013: Ice-shelf melting around Antarctica. *Science*, **341**, 266–270, https://doi.org/10.1126/science.1235798.

Rintoul, S. R., A. Silvano, B. Pena-Molino, E. van Wijk, M. Rosenberg, J. S. Greenbaum, and D. D. Blankenship, 2016: Ocean heat drives rapid basal melt of the Totten Ice Shelf. *Sci. Adv.*, **2**, e1601610, https://doi.org/10.1126/sciadv.1601610.

Rodriguez, A. R., M. R. Mazloff, and S. T. Gille, 2016: An oceanic heat transport pathway to the Amundsen Sea embayment. *J. Geophys. Res. Oceans*, **121**, 3337–3349, https://doi.org/10.1002/2015JC011402.

Schmidtko, S., K. J. Heywood, A. F. Thompson, and S. Aoki, 2014: Multidecadal warming of Antarctic waters. *Science*, **346**, 1227–1231, https://doi.org/10.1126/science.1256117.

Silvano, A., S. Rintoul, and L. Herraiz-Borreguero, 2016: Ocean-ice shelf interaction in East Antarctica. *Oceanography*, **29**, 130–143, https://doi.org/10.5670/oceanog.2016.105.

——, S. R. Rintoul, B. Peña-Molino, and G. D. Williams, 2017: Distribution of water masses and meltwater on the continental shelf near the Totten and Moscow University ice shelves. *J. Geophys. Res. Oceans*, **122**, 2050–2068, https://doi.org/10.1002/2016JC012115.

Smith, R. D., M. E. Maltrud, F. O. Bryan, and M. W. Hecht, 2000: Numerical simulation of the north Atlantic ocean at 1/10° *J. Phys. Oceanogr.*, **30**, 1532–1561, https://doi.org/10.1175/1520-0485(2000)030<1532:NSOTNA>2.0.CO;2.

——, and Coauthors, 2010: The Parallel Ocean Program (POP) reference manual ocean component of the Community Climate System Model (CCSM) and Community Earth System Model (CESM). Rep. LAUR-01853, 141 pp., http://www.cesm.ucar.edu/models/cesm1.0/pop2/doc/sci/POPRefManual.pdf.

Spence, P., S. Griffies, M. England, A. Hogg, O. A. Saenko, and N. C. Jourdain, 2014: Rapid subsurface warming and circulation changes of Antarctic coastal waters by poleward shifting winds. *Geophys. Res. Lett.*, **41**, 4601–4610, https://doi.org/10.1002/2014GL060613.

——, R. M. Holmes, A. M. Hogg, S. M. Griffies, K. D. Stewart, and M. H. England, 2017: Localized rapid warming of West Antarctic subsurface waters by remote winds. *Nat. Climate Change*, **7**, 595–603, https://doi.org/10.1038/nclimate3335.

Stewart, A. L., and A. F. Thompson, 2015: Eddy-mediated transport of warm circumpolar deep water across the Antarctic shelf break. *Geophys. Res. Lett.*, **42**, 432–440, https://doi.org/10.1002/2014GL062281.

——, A. Klocker, and D. Menemenlis, 2018: Circum-Antarctic shoreward heat transport derived from an eddy- and tide-resolving simulation. *Geophys. Res. Lett.*, **45**, 834–845, https://doi.org/10.1002/2017GL075677.

——, ——, and ——, 2019: Acceleration and overturning of the Antarctic Slope Current by winds, eddies, and tides. *J. Phys. Oceanogr.*, **49**, 2043–2074, https://doi.org/10.1175/JPO-D-18-0221.1.

Thompson, A. F., K. J. Heywood, S. Schmidtko, and A. L. Stewart, 2014: Eddy transport as a key component of the Antarctic overturning circulation. *Nat. Geosci.*, **7**, 879–884, https://doi.org/10.1038/ngeo2289.

——, A. L. Stewart, P. Spence, and K. J. Heywood, 2018: The Antarctic Slope Current in a changing climate. *Rev. Geophys.*, **56**, 741–770, https://doi.org/10.1029/2018RG000624.

Wåhlin, A. K., R. D. Muench, L. Arneborg, G. Björk, H. K. Ha, S. H. Lee, and H. Alsén, 2012: Some implications of Ekman layer dynamics for cross-shelf exchange in the Amundsen Sea. *J. Phys. Oceanogr.*, **42**, 1461–1474, https://doi.org/10.1175/JPO-D-11-041.1.

Walker, D. P., A. Jenkins, K. M. Assmann, D. R. Shoosmith, and M. A. Brandon, 2013: Oceanographic observations at the shelf break of the Amundsen Sea, Antarctica. *J. Geophys. Res. Oceans*, **118**, 2906–2918, https://doi.org/10.1002/jgrc.20212.

Webb, D. J., R. M. Holmes, P. Spence, and M. H. England, 2019: Barotropic Kelvin wave-induced bottom boundary layer warming along the west Antarctic Peninsula. *J. Geophys. Res. Oceans*, **124**, 1595–1615, https://doi.org/10.1029/2018JC014227.

Williams, R. G., C. Wilson, and C. W. Hughes, 2007: Ocean and atmosphere storm tracks: The role of eddy vorticity forcing. *J. Phys. Oceanogr.*, **37**, 2267–2289, https://doi.org/10.1175/JPO3120.1.

Wunsch, C., 2011: The decadal mean ocean circulation and Sverdrup balance. *J. Mar. Res.*, **69**, 417–434, https://doi.org/10.1357/002224011798765303.

Yeager, S., 2013: Understanding and predicting changes in North Atlantic sea surface temperature. Ph.D. thesis, University of Colorado, 176 pp.

——, 2015: Topographic coupling of the Atlantic overturning and gyre circulations. *J. Phys. Oceanogr.*, **45**, 1258–1284, https://doi.org/10.1175/JPO-D-14-0100.1.